

# COMPUTATIONAL INVESTIGATION OF MICRO-SCALE SHROUDED ROTOR AERODYNAMICS IN HOVER

Vinod K. Lakshminarayan \*

James D. Baeder †

Alfred Gessow Rotorcraft Center  
Department of Aerospace Engineering  
University of Maryland  
College Park, MD 20742.

## Abstract

In this work, a compressible Reynolds Averaged Navier Stokes (RANS) solver is used to investigate the aerodynamics of a micro-scale shrouded rotor configuration in hover; in order to evaluate the predictive capability of the computational approach and to understand the flow physics of the micro-scale shrouded systems. The overall performance is well predicted for a range of RPMs. The shrouded configuration shows improved performance over the free rotor, mainly seen as an increase in thrust. The thrust produced by the rotor in the shrouded configuration is lower than that of the free rotor, but the thrust generated by the shroud more than compensates for the deficit. The thrust produced from the shroud is identified to come from two main sources. First, the low pressure created primarily by the blades and partly by the tip vortex around the shroud inlet generates large shroud thrust at sections near the blade location. Second, the suction created due to the flow accelerating around the shroud inlet generates additional thrust, and becomes the primary source of thrust production at shroud sections away from the blades. The low pressure due to the tip vortex can help in enhancing the flow acceleration. A study of the effect of various shroud parameters show that diffuser angle and diffuser length did not have much influence on the performance of the system, while smaller tip clearance and use of elliptic shroud inlet significantly improve the overall performance. Finally, an improved shroud design is proposed that might be better suited for non-hovering flight conditions.

## Nomenclature

$a_w$	wake contraction area ratio
$C_P$	power coefficient = $\text{power}/(\rho\pi R^2 U_{tip}^3)$
$C_{P_{ideal}}$	ideal power coefficient = $C_T^{3/2}/\sqrt{2}$
$C_T$	thrust coefficient = $\text{thrust}/(\rho\pi R^2 U_{tip}^2)$
$c$	chord length of the airfoil, $m$
$D_t$	throat diameter, $m$
$FM$	figure of merit = (ideal power)/(actual power) = $C_{P_{ideal}}/C_P$
$L_d$	diffuser length of the shroud, $m$
$p$	pressure, $N/m^2$
$p_\infty$	freestream pressure, $N/m^2$
$q$	non-dimensionalized second invariant of the velocity gradient tensor, $\frac{\partial u_i}{\partial x_j} \frac{\partial u_j}{\partial x_i}$ (normalized by tip speed and blade chord)
$R$	radius of the rotor, $m$
$r$	radial location of the blade, $m$
$r_{tip}$	tip radius of the shroud, $m$
$U_r, U_z$	radial and inflow velocities, $m/s$

$U_{tip}$	tip speed, $m/s$
$x, y, z$	Cartesian coordinates
$\delta_{tip}$	tip clearance of the shroud, $m$
$\theta$	azimuth location, deg
$\theta_d$	twice the expansion angle of the shroud, deg

## Introduction

Micro Air Vehicles (MAVs), as defined in the research program of Defense Advanced Research Projects Agency (DARPA), are cheap flying vehicles with no dimension exceeding 6 inches (15 cm), with a weight of no more than 100 grams. The endurance is encouraged to be one hour and the payload should include a camera or other sensing devices. Over the past decade, MAVs have received an increasing amount of attention in military and civilian markets.

While there is no perfect MAV for all situations, most of the small flying vehicles being developed can be divided into three categories - fixed wing, flapping wing and rotary wing. Fixed-wing MAVs have so far been the most successful at achieving the longest endurance and greatest speed and range. However, they are not hover capable and therefore cannot perform indoor missions ef-

\* Research Associate, vinodkl@umd.edu

† Associate Professor, baeder@umd.edu

fectively. Both flapping wing and rotary wing MAVs provide hover capability. However, due to their complex kinematics, hovering flapping-wing vehicles have very poor mechanical efficiency. On the other hand, rotary-wing vehicles can adapt some of the technology used in full-scale vehicles and can keep the mechanical losses to a minimum. However, current day rotary wing vehicles are still not efficient enough to meet the objectives set by DARPA.

The main difficulty in achieving better performance with rotary wing vehicles come from the large hover power requirements. Hover is an intrinsically high-power flight state with considerably larger energy requirements than cruise for fixed wing vehicles; this fact is independent of scale. If hover extends for a significant fraction of the mission duration, hover efficiency becomes a key vehicle characteristic that must be carefully addressed. Good hovering efficiency requires good aerodynamic efficiency.

MAVs have relatively poor aerodynamic efficiency compared to full-scale vehicles. MAV rotors have achieved a maximum Figure of Merit ( $FM$ ) of around 0.6 while full-scale helicopters may have a maximum  $FM$  near 0.8 or higher. This degraded performance is due to the adverse effects of the low Reynolds numbers at which the MAVs operate. Rotary-wing MAVs generally have tip Reynolds number of the order of 20,000 to 100,000. At these low Reynolds numbers, viscous effects in the flow are dominant over the inertial ones, boundary layers are thick and undergo several complex phenomena. Separation, transition, and reattachment can all occur within a short chordwise distance, forming laminar separation bubbles that have a strong adverse effect on the lifting surface characteristics.

One of the possible technological solution to enhance the aerodynamic performance and payload capability of rotary wing MAV is to enclose the rotor with a duct or a shroud. Since the 1930s, the propeller industry has been using ducts to enclose the propeller to improve its power loading (Refs. 1–3). The concept of utilizing a duct is also popular in fenestron tail rotors (Refs. 4, 5) and has been recently applied to ducted fan/rotor VTOL UAVs (Refs. 6, 7). The use of a duct/shroud also promises to enhance the capabilities of a hovering MAV rotor. In addition to improving the aerodynamic performance, the shroud can serve as a safety feature, protecting the rotating blades and also offers the possibility of attenuating the noise signature of the rotor.

Even though a considerable amount of work, both experimental and analytical, has been performed on ducted rotors, these investigations are predominantly for scales that are much larger than MAVs. The physical understanding gained from these studies may or may not be applicable to shrouded rotors operating in the viscous

dominated low Reynolds number flow regime. Therefore, one needs to carefully investigate the benefits of using a shroud at MAV-scale. Recently, Pereira and Chopra (Refs. 8, 9) performed an extensive parametric study on the performance of small-scale shrouded rotors and demonstrated the merits of this concept at MAV scale. Experiments were performed investigating the effects of varying diffuser expansion angle, diffuser length, inlet lip radius, and blade tip clearance of the shroud. Based on the suggestions from Pereira and Chopra, Hrishikeshavan and Chopra (Ref. 10) built a shrouded rotor MAV and obtained significant performance benefits.

Although the parametric study of Pereira and Chopra (Refs. 8, 9) is very extensive, there is still significant scope in improving the shroud design at these scales. However, it is extremely time consuming to experimentally study the effects of various shroud parameters. Instead, computational fluid dynamics (CFD) can be used to study the performance and flow physics of micro-scale shrouded rotor and can thereby be used to aid in the design process. Previous work by the present authors (Refs. 11, 12) demonstrated the capability of using a compressible Reynolds Averaged Navier-Stokes (RANS) solver to study the flow physics of hovering micro-rotors. The studies provided good performance and flow-field prediction. Following this, Lummer (Ref. 13) initiated the computational study of micro-scale shrouded rotor in hover. However, Lummer assumed the shroud to be rotating with the rotor, which relaxed the need for a time accurate computation.

The present work seeks to extend the methodology developed in previous studies to perform time-accurate simulation of a hovering micro-scale shrouded rotor. Experimental results obtained by Hrishikeshavan and Chopra (Ref. 10) will be used for validation followed by detailed analysis of the flow physics. Finally, investigation on the effect of diffuser angle, tip clearance and shroud leading edge shape will be performed.

## Rotor and Shroud Configuration

The experimental data of Hrishikeshavan and Chopra (Ref. 10) on a two-bladed hovering shrouded rotor is used for performance validation. The experimental setup is shown in Fig. 1. The blades used have a 2 : 1 taper starting at the 60% span location with the leading edge remaining straight and the trailing edge tapering towards the leading edge; this results in a nose down twist in this region due to the camber. The radius and the chord of the blade are 121mm and 25mm, respectively, making the aspect ratio equal to 4.84. A circular arc airfoil with 10% camber, 2% thickness and leading edge



Figure 1: Experimental setup of Hrishikeshavan and Chopra (Ref. 10).

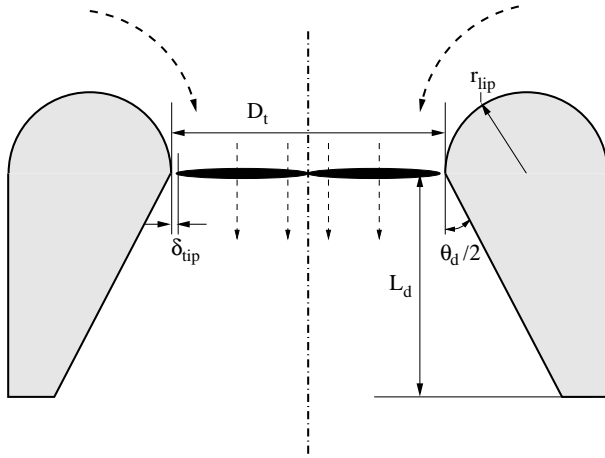


Figure 2: Schematic of cross sectional view of shrouded-rotor.

sharpened from the 8% chord location is used.

The major dimension that defines the shroud geometry is the throat diameter ( $D_t$ ). A schematic of the cross-sectional view of a shrouded-rotor is displayed in Fig. 2. The throat diameter is defined as the inner diameter of the shroud at the rotor-blade plane. The shroud consists of two sections with the rotor blade plane as the line of demarcation between the sections. The section of the shroud above the rotor blades in Fig. 2 is the inlet, and the section below the rotor blade plane is the diffuser. The inlet consists of a semi-circle and the exterior is known as the lip with the lip radius denoted by  $r_{lip}$ . The diffuser has two parameters that define it, which are its length,  $L_d$ , and its expansion angle,  $\theta_d/2$ .

The throat diameter used by Hrishikeshavan and Chopra (Ref. 10) is  $247\text{cm}$ , which makes the tip clearance equal to  $2.5\text{mm}$  (1% of throat diameter). The lip radius and the diffuser length are 9% and 15%, respectively, of the throat diameter. The diffuser angle is  $0^\circ$ . Note that some of the dimensions reported in the original paper might be slightly different due to measurement errors.

## Methodology

The computations are performed using the overset structured mesh solver OVERTURNS (Ref. 20). All the computations are performed in a time-accurate manner in the inertial frame of reference, such that the blades rotate while the shroud remains stationary. The code solves the compressible RANS equations using a preconditioned dual-time scheme in the diagonalized approximate factorization framework, described by Buelow et al. (Ref. 15) and Pandya et al. (Ref. 16). The diagonal form of implicit approximate factorization method was originally developed by Pulliam and Chaussee (Ref. 17). The low Mach preconditioning is based on the one developed by Turkel (Ref. 18). The preconditioning is used not only to improve convergence but also to improve the accuracy. The inviscid terms are computed using a third order MUSCL scheme utilizing Koren's limiter with Roe's flux difference splitting and the viscous terms are computed using second order central differencing. The Spalart-Allmaras (Ref. 19) turbulence model is employed for the RANS closure. This one-equation model has the advantages of ease of implementation, computational efficiency and numerical stability. The production term in this eddy-viscosity model is modified (Ref. 20) to account for the reduction of turbulence in the vortex core due to flow rotation effects. The downwash velocity in the bottom plane of the rotor can be significant. In order to account for this and to properly represent the inflow at the other far-field boundaries, the point-sink boundary condition approach of Srinivasan et al. (Ref. 21) is used.

For the purpose of modeling, the outer portion of the shroud is closed using a spline fit (experiments use an open-ended shroud), which facilitates the use of a C-type mesh. This modification should not change the overall flow physics and performance data, as the flow is mostly quiescent at the outer portion of the shroud in hover. For all the shrouded rotor computations, a four mesh overset system consisting of two C-O type blade meshes, a C-H type shroud mesh and a cylindrical background mesh is used. The blade and the shroud meshes conform to their respective bodies. Information is exchanged from one grid to the other using chimera interpolations. Implicit hole-cutting technique (Ref. 22) is used to find the con-

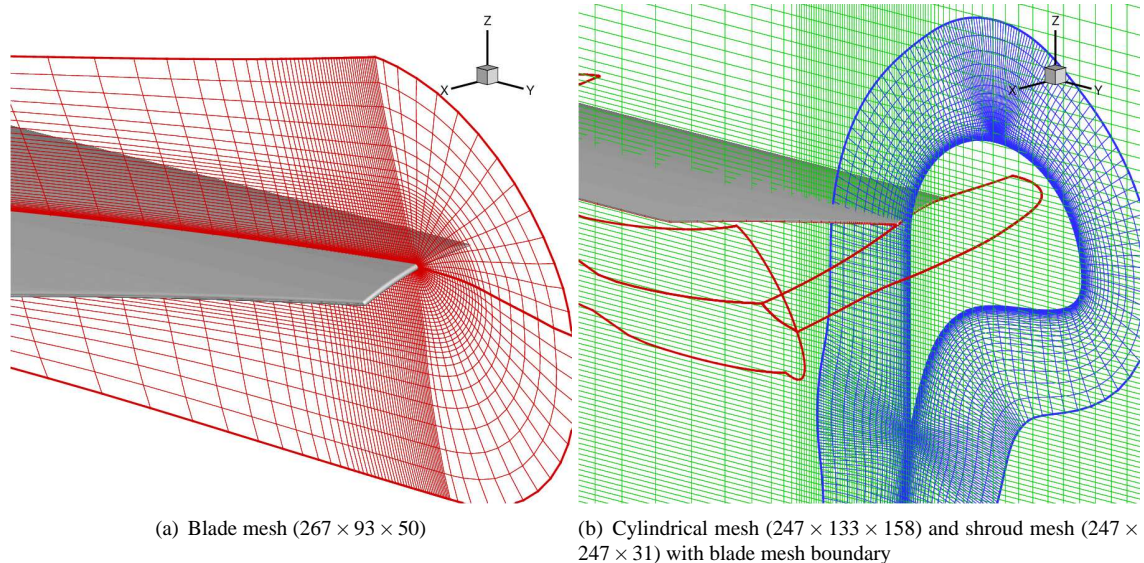


Figure 3: Computational mesh for shrouded-rotor calculation.

nectivity information between various overset meshes. Each of the blade meshes have  $267 \times 93 \times 50$  points in the streamwise, spanwise and normal directions respectively, the shroud mesh has  $247 \times 247 \times 31$  in the azimuthal, wrap-around and normal directions, respectively and the background cylindrical mesh has  $247 \times 133 \times 158$  points in the azimuthal, radial and vertical directions respectively, see Fig. 3. The total number of mesh points used is approximately 10 million. In the most refined regions, the background mesh has a grid spacing of 0.025 chords in the radial and 0.04 chords in the vertical directions. Along the azimuthal direction, a grid plane is spaced every  $1.5^\circ$ . The chosen time-step size corresponds to a motion of  $0.25^\circ$  of azimuth. Each simulation is run for 8 revolutions to achieve convergence.

## Results

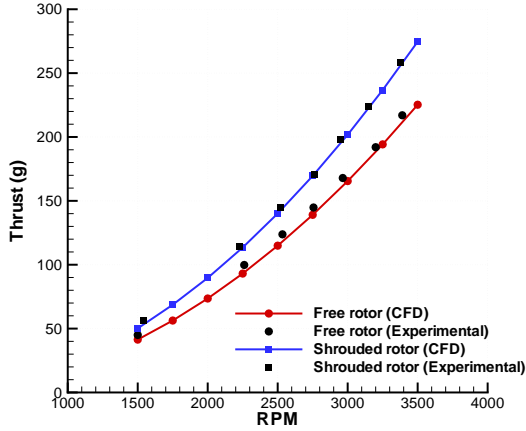
### Performance Comparison

Experiments were conducted for a range of RPM varying from 1500 to 3500. Correspondingly, the tip Reynolds number varied from 30,000 to 70,000 and the tip Mach number ranged from 0.056 to 0.131. The collective setting was set to  $22^\circ$ . Figure 4(a) shows the variation of thrust with rotational speed obtained from computation as well as experiments for free (unshrouded) and shrouded rotors. Clearly, the computational results agree very well with the experimental data for both the rotors. The improvement in thrust produced by using a shroud is clearly noticeable. Figure 4(b) compares the power curves obtained from computations with those measured from ex-

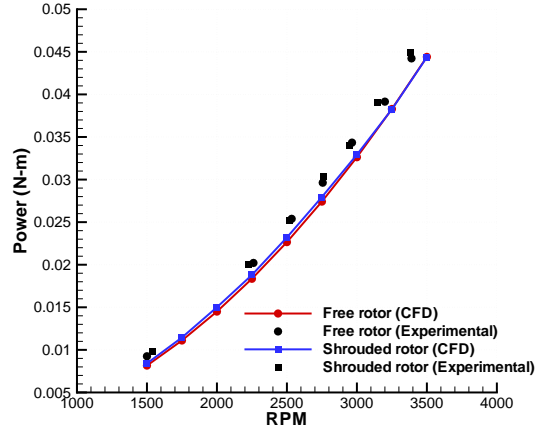
periments as a function of RPM. The powers obtained from the computations are seen to be marginally lower than the experimental values at all RPMs for both the rotors. Interestingly, the experimental power required by the shrouded rotor is similar to that for the free-rotor at all RPMs; such a trend is also well captured by the computations. The difference in the computed power for the free and the shrouded configuration is less than 4% at all rotational speeds. The results demonstrate the capability of the current computational study to provide good performance predictions.

### Collective Sweep

Following the validation of the computational methodology, calculations are done for a range of rotor collective settings at a fixed RPM of 2500. Figure 5(a) shows the CFD predicted variation of the free rotor thrust coefficient ( $C_T$ ) with collective setting. In addition, the total thrust coefficient for the shrouded rotor is shown along with the individual thrust coefficients for the shroud and rotor. Clearly, the shrouded rotor combination produces larger thrust as compared to that from the free rotor at all collective settings, with the difference more pronounced at higher values ( $\sim 30\%$  higher at  $26^\circ$  collective angle compared to  $\sim 8\%$  higher at  $14^\circ$  collective angle). Interestingly, the thrust produced by the rotor in the shrouded configuration is lower than that produced by the free rotor. Similar observations were made by Pereira and Chopra (Ref. 9) in their experimental studies. The thrust produced by the shroud more than compensates the deficit produced by the rotor to produce a net increase in thrust for the shrouded configuration.



(a) Thrust versus RPM



(b) Power versus RPM

Figure 4: Performance comparison between CFD predictions and experiment as a function of RPM for micro-scale free and shrouded rotor.

A better understanding of the contribution of the shroud to the total thrust of the shrouded rotor can be obtained by looking at the ratio of shroud thrust to the total thrust, computed as a function of collective setting, plotted in Fig. 5(b). While the shroud contributes to about 19% of the total thrust at lower collective setting, it increases to as high as 29% of the total thrust at the highest collective setting. Note that these ratios can vary based on the shroud geometry, but the trend of increasing shroud contribution with increasing rotor collective setting should hold true for any shroud geometry as long as there is no significant flow separation.

Figure 5(c) shows the variation of power coefficient ( $C_P$ ) with rotor collective setting for both free as well as shrouded rotor. It should be noted that the power contribution for the shrouded rotor configuration comes only from the rotor. The shroud power is almost zero because of the radial symmetry. Surprisingly, as seen from the plot, the power required for both the free as well as the shrouded rotors are almost identical (within 5%) at all collective settings. Similar observations were made earlier while looking at the effect of RPM. As a result, the increase in thrust obtained for the shrouded rotor at a constant collective angle almost corresponds to performance gain at a constant power setting.

A measure of efficiency is obtained by looking at the figure of merit ( $FM$ ), defined by the ratio of ideal power to actual power, as a function of thrust coefficient, plotted in Fig. 5(d). For the purpose of comparison, the ideal power for the shrouded rotor is assumed to be the same as that for a free rotor operating at the same thrust. From the plot, the shrouded rotor is seen to achieve a maximum  $FM$  of about 0.78, whereas the free rotor  $FM$  saturates at

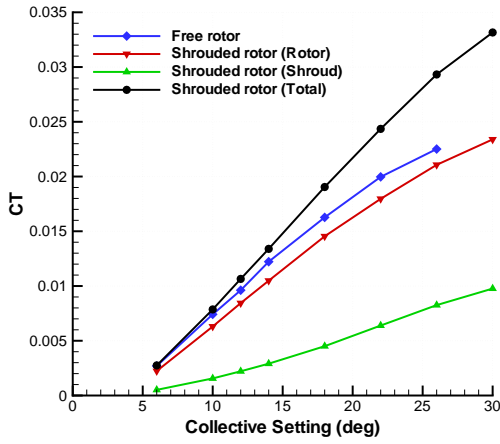
around 0.6. Also, the shrouded rotor sustains high  $FM$  for a larger range and for higher values of thrust coefficient compared to the free rotor. Similar observations are made for the ratio of thrust to power coefficients (power loading), shown in Fig. 5(e). The reason for high efficiency even at large collective angles is because of the off-loading of thrust from the rotor (seen earlier) in the shrouded configuration, which allows the rotor to operate at a much higher collective angle without stalling. Therefore, enclosing the rotor with a shroud not only improves the performance, but also allows the rotor to operate at a much higher thrust, thereby improving the overall capability of the MAV. However, it must be kept in mind that, the increase in thrust obtained by a shrouded rotor must also compensate for the weight of the shroud added to the MAV.

## Understanding the Physics

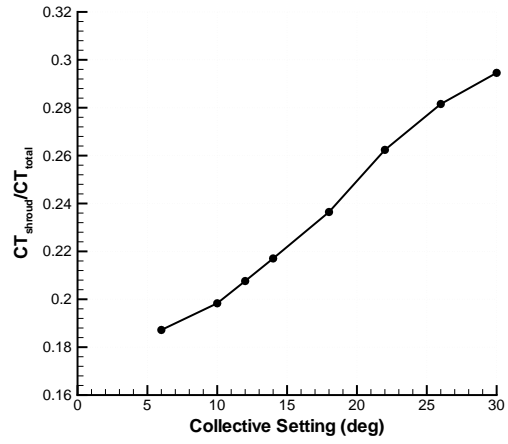
Although, the flow-field predicted by CFD simulations can be used to provide the integrated performance of the rotor and shroud for comparison with experimental measurements, they also provide a wealth of high resolution information that can be explored to obtain a better understanding of the reasons behind the performance benefits of the shroud.

### Rotor and Shroud Performance

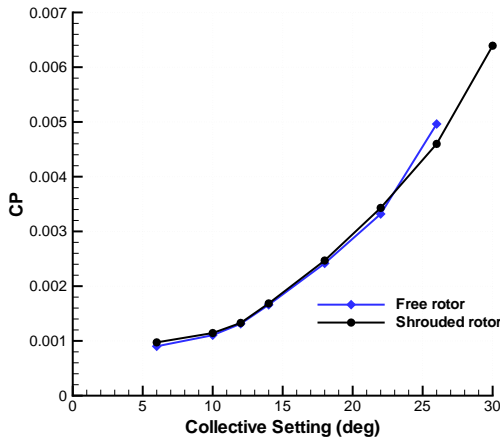
A better understanding of the rotor performance in the shrouded configuration can be obtained by looking at the spanwise distribution of the integrated quantities and comparing it with the distribution for the free rotor. Fig-



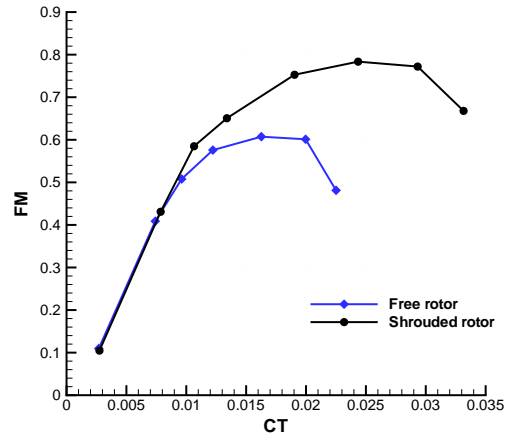
(a)  $C_T$  versus collective setting



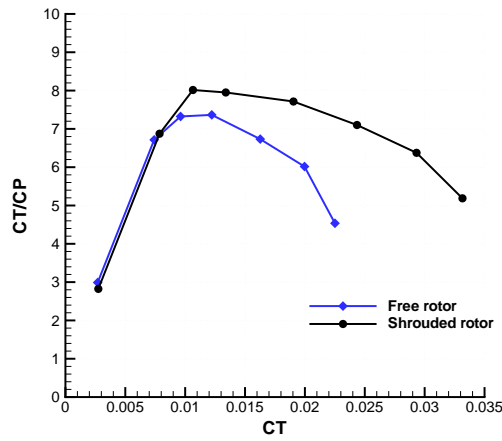
(b)  $C_{T_{shroud}}/C_{T_{total}}$  versus collective setting



(c)  $C_P$  versus collective setting

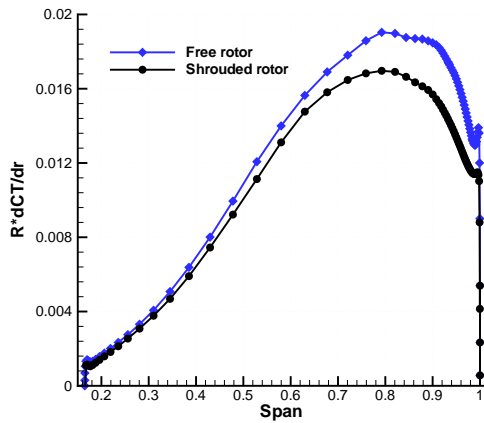


(d)  $FM$  versus  $C_T$

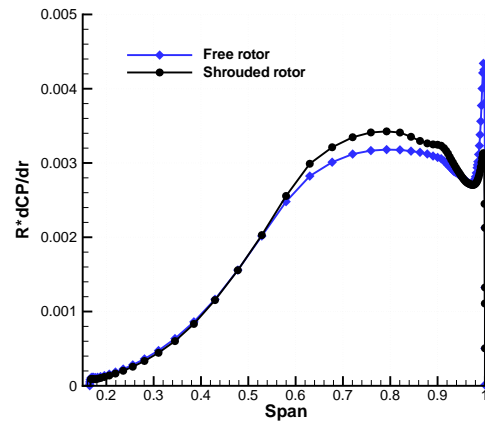


(e)  $C_T/C_P$  versus  $C_T$

Figure 5: CFD predicted performance as a function of collective setting for micro-scale free and shrouded rotors.

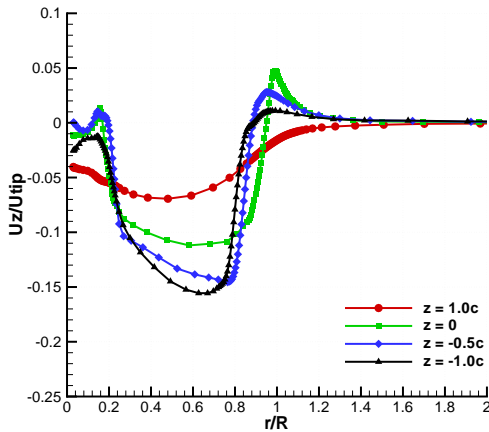


(a) Thrust distribution

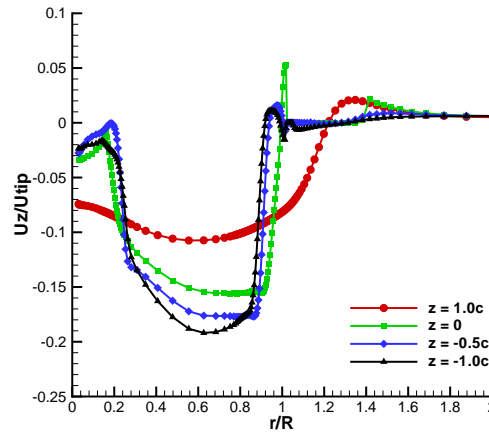


(b) Power distribution

Figure 6: CFD predicted spanwise rotor thrust and power distribution,  $22^\circ$  collective setting.



(a) Free rotor



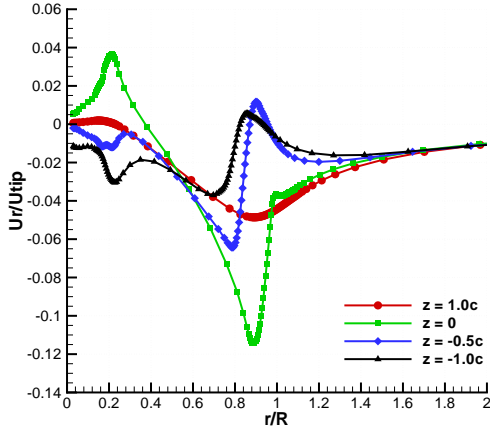
(b) Shrouded rotor

Figure 7: CFD predicted average inflow (non-dimensionalized by tip speed) along radial direction at different planes above and below the rotor,  $22^\circ$  collective setting.

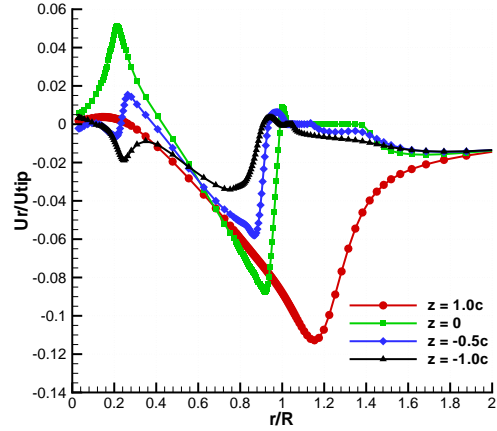
Figure 6 shows the spanwise thrust and power distribution at  $22^\circ$  collective setting for both the configurations. As seen earlier, the thrust produced by the rotor in the shrouded configuration is lower compared to that of the free rotor and the difference occurs throughout the span, but is more prominent in the outboard region of the blade. On the other hand, the difference in power is marginal and occurs more towards the tip of the blade. Note that, for the present flow condition, the computed integrated power for the shrouded rotor is  $\sim 4\%$  more than that for the free rotor. It should be mentioned here that, the overall shape of the thrust and power distributions are not too different for the two configurations. This suggests that

the rotor blade for the shrouded configuration can possibly be designed without the consideration of the shroud geometry; the blades that perform well for a free rotor should provide good performance even with the use of a shroud.

The difference between the blade performance in the free and the shrouded rotor configurations can be comprehended by looking at the inflow. Figures 7(a) and (b) respectively, show the radial variation of the inflow velocity averaged in the azimuthal direction for the free and the shrouded rotors. The variation is shown at different planes above and below the rotor. The value of  $z$  is positive above the rotor plane and negative below. It



(a) Free rotor



(b) Shrouded rotor

Figure 8: CFD predicted average radial velocities (non-dimensionalized by tip speed) along radial direction at different planes above and below the rotor,  $22^\circ$  collective setting.

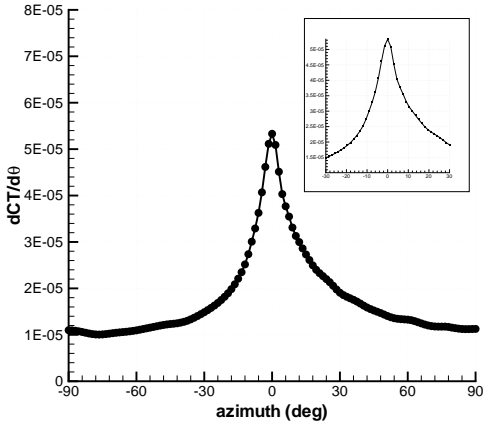


Figure 9: CFD predicted azimuthal variation of shroud thrust,  $22^\circ$  collective setting.

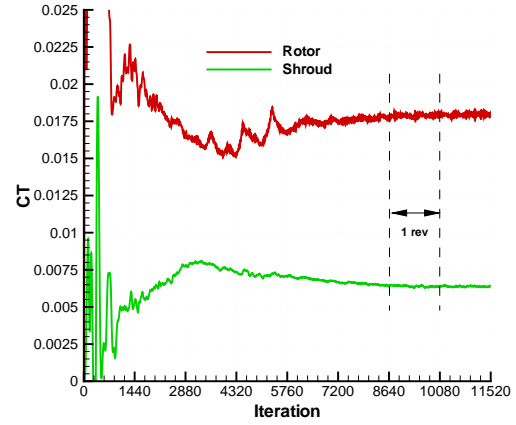


Figure 10: Convergence history of rotor and shroud thrust,  $22^\circ$  collective setting.

should be noted that the results shown at  $z = 0$  are obtained by averaging those at  $z = 0.1c$  and  $z = -0.1c$  (to minimize influence of the rotor blade). The velocities are non-dimensionalized by the tip speed. Clearly, the inflow for the shrouded configuration is larger at all planes compared to that for the free rotor. As a result, the effective angle of attack seen by the blades in the shrouded configuration is lower, leading to a lower blade thrust. Above the plane of the rotor ( $z = 1.0c$ ), it is seen that the inflow is significantly greater for the shrouded rotor than for the free rotor. Thus, the shroud has significantly accelerated the flow above the rotor downward through the shroud

and then into the rotor plane. Note that at the plane of the rotor and at  $z = -0.5c$ , the downwash velocity is zero at some locations due to the blockage of the shroud. A small amount of upwash is noticeable outside the shroud.

Looking at the radial component of the average velocities at different planes, shown in Fig. 8, the magnitude of the velocity pointing inboard is larger for the shrouded configuration as compared to that for the free rotor at a plane above the rotor, while the trend is reversed at the plane of the rotor. At the plane above the rotor, the shroud is perturbing the flow radially inward; while at the plane of the rotor, the shroud blockage inhibits radial

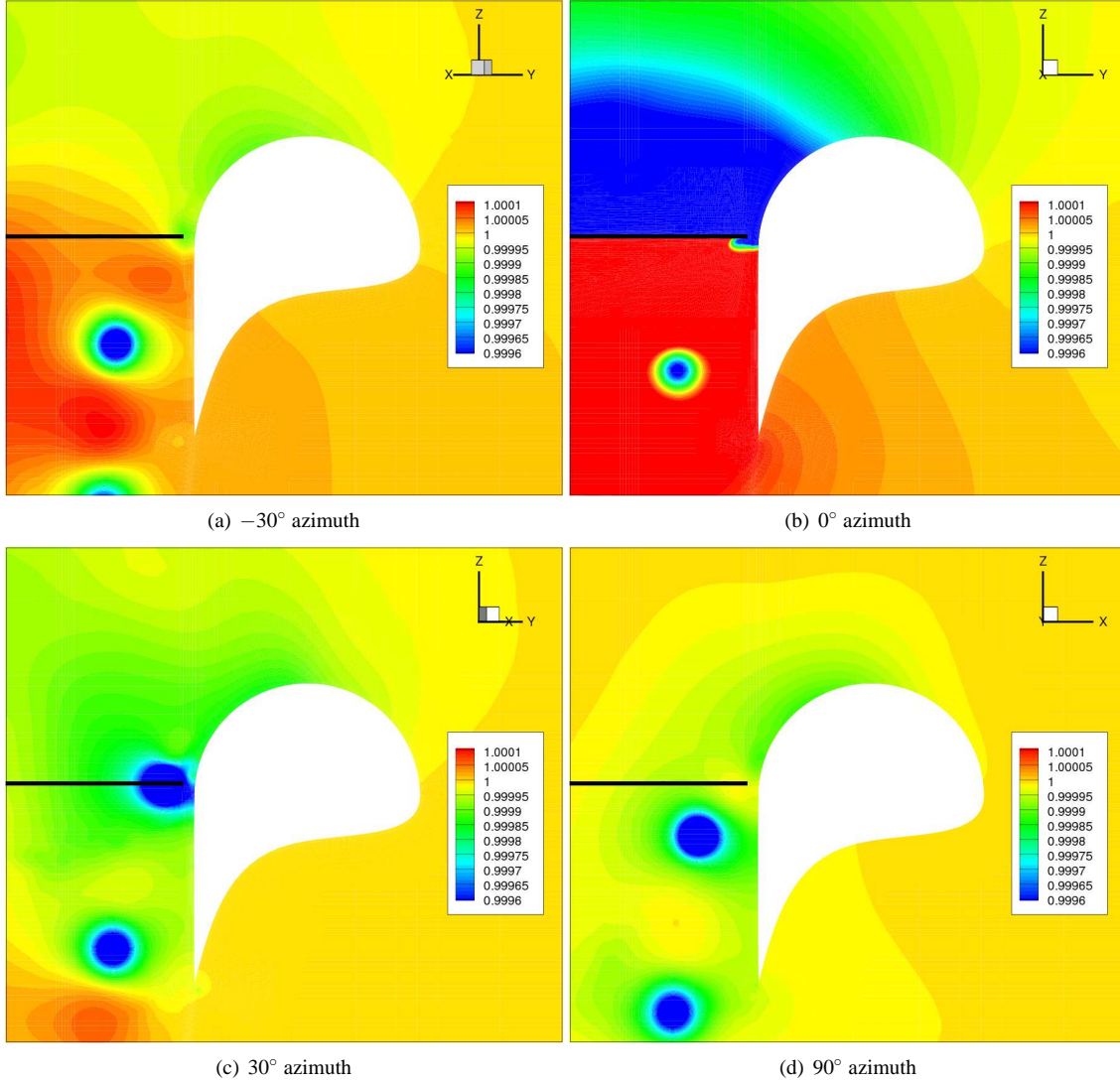


Figure 11: Sectional pressure (non-dimensionalized by freestream value) contour at different azimuth location for micro-scale shrouded rotor,  $22^\circ$  collective setting. Plane of the rotor is shown in black.

flow. There is not much difference in the radial velocities below the rotor plane.

To understand the performance of the shroud, azimuthal variation of the shroud thrust at one instant of time is plotted for  $22^\circ$  collective angle in Fig. 9. The  $0^\circ$  azimuth corresponds to the location of the blade and the azimuth increases with the increasing wake age. As expected, the thrust produced by different sections of the shroud are not similar. The thrust peaks at the section where the blade is present and drops by about 5 times at the  $90^\circ$  and  $-90^\circ$  azimuthal planes, which are the locations furthest from the blade. An interesting feature to notice is that the thrust drops at different rates on the either sides of the blade location. This can be more clearly seen in the zoomed-in figure. The thrust in the positive

azimuth location drops at a slower rate compared to that in the negative azimuth location. Similar trends were observed for all the collective settings. The reason for this will be explained later in this section. Although, the thrust varies at different azimuthal sections of the shroud, the average thrust of the shroud and the rotor remains fairly constant with time. This can be seen from the convergence history plot of the shroud and rotor thrusts plotted in Fig. 10. Note that the rotor and shroud thrusts have fluctuations on the order of 2% and 1%, respectively. The rotor power has a fluctuation of  $\sim 4\%$ . These fluctuations are due to unsteadiness in the flow-field at these low Reynolds numbers. Details of the unsteadiness are provided in an earlier paper (Ref. 11) by the current authors.

A better understanding of the azimuthal thrust distri-

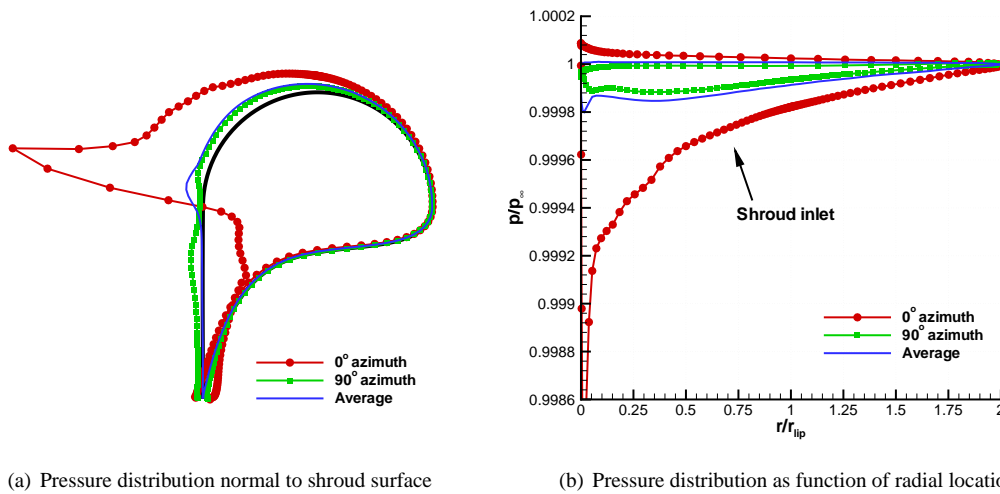


Figure 12: CFD predicted sectional and average pressure (non-dimensionalized by freestream value) distribution on the shroud, 22° collective setting.

bution can be obtained by looking at the pressure contour plots. Figure 11 shows the sectional pressure (non-dimensionalized by freestream value) contours at azimuth locations of  $-30^\circ$ ,  $0^\circ$ ,  $30^\circ$  and  $90^\circ$ . From the plot, it is apparent that the peak seen in the shroud thrust at  $0^\circ$  azimuth location is due to the large low pressure created by the rotor on its upper surface, which extends to the inlet region of the shroud and also partly due to the high pressure created on the lower surface of the blade, which extends to the outer portion of the blade. As one moves away from the blade, the pressure difference created by the rotor blade decreases and the suction generated by the flow accelerating around the shroud inlet becomes the primary contributor to the shroud thrust. The difference in the shroud thrust drop on the either side of the blade location can be understood by looking at the pressure contours at  $30^\circ$  and  $-30^\circ$  azimuthal plane. At  $30^\circ$  azimuthal location, the tip vortex lingers around the rotor plane, which not only aids in the acceleration of the flow over the duct, but also creates a low pressure region on the shroud inlet. On the other hand, the tip vortex at the  $-30^\circ$  azimuth location has a wake age of  $150^\circ$  and therefore, has convected to a position much below the rotor plane. The tip vortex at this location does not have as significant an influence on the flow-field near the shroud inlet as was seen at the  $30^\circ$  azimuth location, thus resulting in a lower sectional thrust. At  $90^\circ$  azimuth location, although the flow might be accelerated better over the shroud compared to the  $-30^\circ$  azimuth location, the pressure difference created by the rotor blades are minimal. As a result,  $-30^\circ$  azimuth location produces slightly higher thrust compared to the  $90^\circ$  azimuthal section.

Figure 12 shows the sectional ( $0^\circ$  and  $90^\circ$  azimuth) as well as azimuthally averaged surface shroud pressure distribution. In Fig. 12(a), a length proportional to the actual pressure is plotted normal to the shroud surface, with higher than freestream pressure pointing in and lower than freestream pressure pointing out. Figure 12(b) plots the variation of pressure (non-dimensionalized by freestream pressure) in terms of the non-dimensional radial location. The radial location is non-dimensionalized by the lip radius of the shroud. The leading edge of the shroud corresponds to  $r/r_{lip} = 1$ . Plotted this way, the area under the curve is proportional to the sectional thrust of the shroud. As seen earlier, the magnitude of low pressure on the shroud inlet at  $0^\circ$  azimuth location is much larger due to the presence of the rotor blade. The large low pressure created by the tip vortex near the plane of the blade is clearly visible at  $0^\circ$  azimuth location. However, the force component due to this low pressure acts mainly in the radial direction and does not contribute much to the shroud thrust. The low pressure developed near the leading edge of the shroud (at the top of the inlet) due to flow acceleration is seen at both azimuth locations and has most of its component in the thrusting direction. The average pressure distribution shows two peaks in the inner portion of the shroud inlet; one due to the suction created by the flow accelerating around the inlet and the other due to the low pressure created by the tip vortex. Pereira and Chopra (Ref. 9) also observed the presence of two peaks in their experimental data. The average pressure on the outer portion of the shroud is close to freestream value and does not affect the shroud performance; therefore, justifying the modification of the outer portion of

the shroud geometry for the purpose of modeling. The diffuser portion of the shroud has higher than freestream pressure at  $0^\circ$  azimuth and lower than freestream pressure at  $90^\circ$  azimuth. However, the average pressure on the diffuser portion is close to freestream value.

As a summary, the thrust produced from the shroud comes from two main sources. First, the low pressure created primarily by the blades and partly by the tip vortex around the shroud inlet generates large shroud thrust at sections near the blade location. Second, the suction created due to the flow accelerating around the shroud inlet generates additional thrust, and becomes the primary source of thrust production at shroud sections away from the blades. The low pressure due to the tip vortex can help in enhancing the flow acceleration.

### Wake Trajectory

A good understanding of the flow physics can be obtained by looking at the tip vortex flow-field. In order to extract only the rotational flow regions and not the highly strained regions, the iso-surfaces of the so-called  $q$ -criterion (Ref. 24) colored with azimuthal vorticity contour is shown in Fig. 13 for the  $22^\circ$  collective setting case. From the plot, the flow-field looks clean and the resolution of the tip vortex until 2 blade passages is clearly evident. Beyond this wake-age, the background mesh becomes too coarse to accurately represent the details of the tip vortex. Although the tip vortex is initially smooth, it is seen to become twisted beginning near the first blade passage. This is because of the fact that it is embedded in a highly strained field due to the presence of the evol-

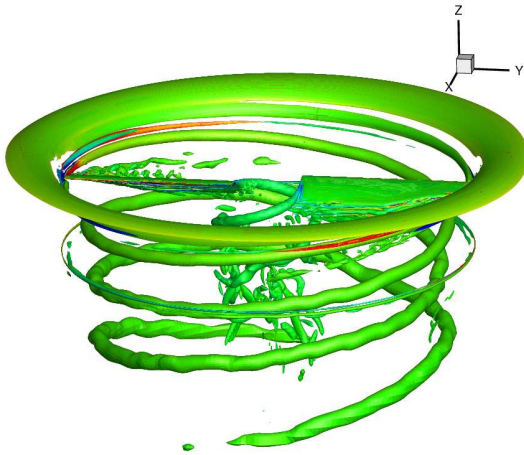
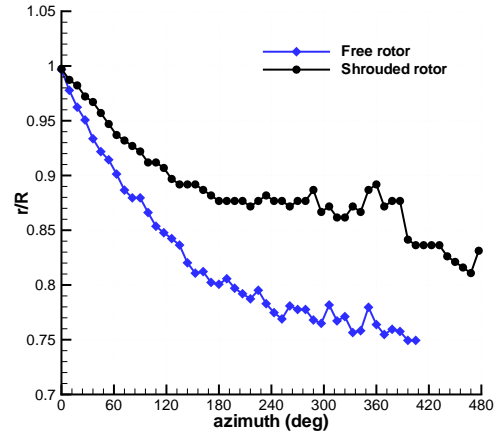
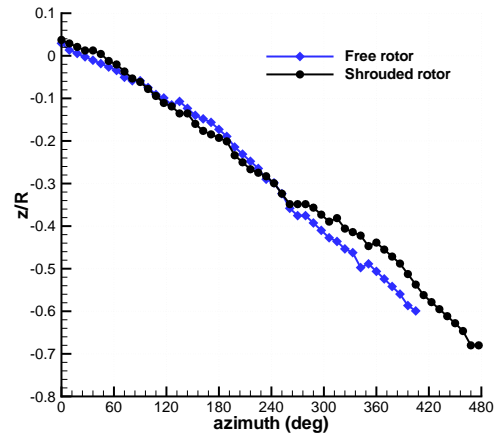


Figure 13: CFD predicted iso-surfaces of second invariant of the velocity gradient tensor,  $q = 0.25$ , colored with azimuthal vorticity contour for baseline micro-scale shrouded rotor,  $22^\circ$  collective setting.



(a) azimuth vs  $r/R$



(b) azimuth vs  $z/R$

Figure 14: CFD predicted wake trajectory for micro-scale shrouded rotor,  $22^\circ$  collective setting.

ing tip vortex. For some of the cases shown later in the paper, the tip vortex stays much closer to the shroud surface and the resulting interaction with the shroud boundary layer generates additional instabilities in the wake. A weak vortex is also seen to be shed from the trailing edge of the shroud.

Figure 14 shows the wake trajectory for the free as well as the shrouded rotor configurations operating at  $22^\circ$  collective setting. As expected, the wake contracts at a much slower rate in the presence of the shroud as compared to from a free rotor. On the other hand, the difference in the vertical convection of the wake of the two configurations is marginal. It should be mentioned here that, according to the momentum theory for the ducted rotors (Ref. 23), the ratio of the shroud thrust to the total thrust is given by

the expression  $1 - \frac{1}{2a_w}$ , where  $a_w$  is the wake contraction area ratio. From the expression, the contribution of the shroud to the total thrust for the shrouded rotor configuration can be calculated to be  $\sim 31\%$  (taking the contraction ratio to be  $\sim 0.85$ ). The CFD predicted value of the shroud contribution to the total thrust is  $\sim 26\%$ . The difference between the ideal momentum theory and the computations can be accounted by the non-ideal contraction of the wake in the CFD calculation. However, the comparison is still reasonable enough, thereby further validating the current calculations. In addition, the expression from the momentum theory suggests that the contribution of the shroud to the total thrust can be increased by having a smaller wake contraction (larger  $a_w$ ). Therefore, for a shrouded rotor configuration with  $0^\circ$  diffuser angle, the best possible shroud sharing of the total thrust is obtained when there is no wake contraction. However, for the present shrouded rotor configuration, the wake contracts fairly significantly. This indicates that the current shroud geometry is far from an optimal design and it should be possible to further improve the performance of a hovering shrouded rotor configuration by using a better shroud shape.

### Effect of Shroud Parameters

To improve the design of the present shroud, it is important to understand the effects of various shroud parameters on the performance and the flow-field of the shrouded rotor configuration. In this section, a study of the effect of tip clearance, diffuser length, diffuser angle and shroud inlet shape is performed. All the parameters are varied independent of each other, so that the individual effects can be isolated.

### Effect of Tip Clearance

Table 1: CFD predicted performance of micro-scale shrouded rotor for different shroud tip clearances,  $22^\circ$  collective setting.

Tip clearance (% $D_t$ )	$C_T$ (rotor)	$C_T$ (shroud)	$C_T$ (total)	$C_P$ (total)
0.5	0.0171	0.0089	0.0260	0.00345
1.0	0.0180	0.0064	0.0244	0.00343
1.5	0.0182	0.0052	0.0234	0.00341
2.0	0.0183	0.0045	0.0229	0.00340
4.0	0.0184	0.0028	0.0212	0.00335
$\infty$	0.0200	0.0000	0.0200	0.00332

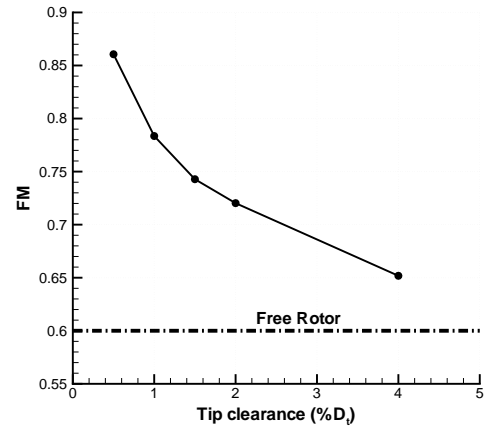


Figure 15: CFD predicted variation of figure of merit with tip clearance for micro-scale shrouded rotor,  $22^\circ$  collective setting.

Table 1 shows the CFD predicted performance variation as a function of shroud tip clearance for the shrouded rotor. The collective angle of the rotor is set to  $22^\circ$ . The baseline configuration corresponds to 1% tip clearance. Also, shown is the performance of the free rotor (tip clearance equals  $\infty$ ). As the tip clearance increases, the rotor thrust increases, while the shroud thrust decreases. However, the decrease in shroud thrust is greater than the increase in rotor thrust, resulting in a net decrease in the total thrust. The total power is also seen to decrease with the increasing tip clearance. To gauge the performance difference between the configurations with various tip clearances, the variation of figure of merit with tip

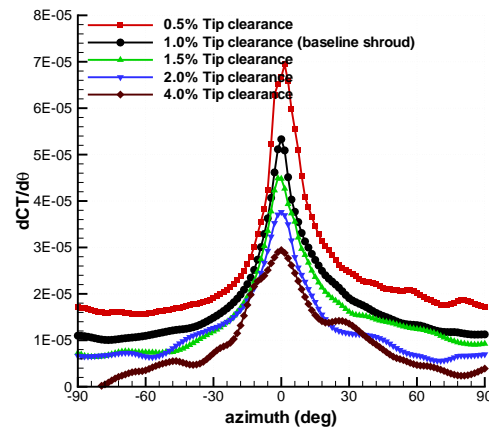


Figure 16: CFD predicted azimuthal variation of shroud thrust for different tip clearances,  $22^\circ$  collective setting.

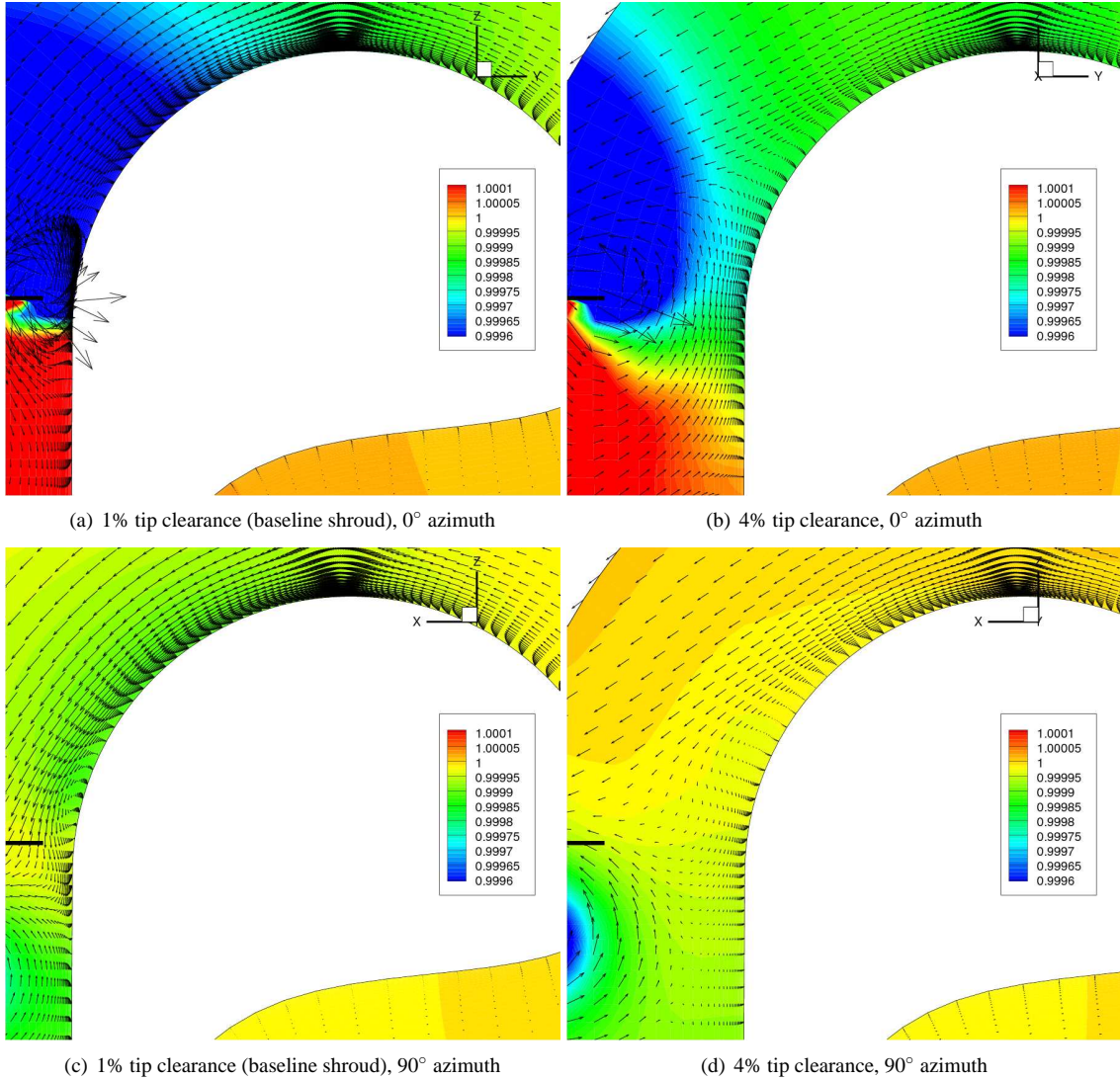


Figure 17: Sectional pressure (non-dimensionalized by freestream value) contour along with velocity vectors for micro-scale shrouded rotor,  $22^\circ$  collective setting. Plane of the rotor is shown in black.

clearance is plotted in Fig. 15. Again, the figure of merit is calculated based on the ideal power required for a free rotor operating at the same thrust. The performance benefit from decreasing tip clearance is clearly evident from this plot. While the configuration with the tip clearance of 0.5% achieves a  $FM$  of about 0.86, the system with the tip clearance of 4% achieves only a  $FM$  close to 0.65. The free rotor achieves a  $FM$  of 0.6. Similar observations were made by Pereira and Chopra (Ref. 8) on the effects of tip clearance.

A better understanding of the differences in the shroud thrust at different tip clearances can be obtained by looking at the azimuthal variation of the shroud thrust at one instant of time for different tip clearance configurations, see Fig. 16. Clearly, as the tip clearance increases

both the peak at  $0^\circ$  azimuth as well as the base value at  $90^\circ$  azimuth decreases. The reason for this can be understood from Fig. 17, which shows the sectional pressure (non-dimensionalized by freestream value) contours along with velocity vectors at  $0^\circ$  and  $90^\circ$  azimuth locations for the configuration with tip clearances of 1% (baseline) and 4%. The plot shows that both the low pressure acting at the shroud inlet at sections near the blade location, as well as the suction generated by flow acceleration around the shroud inlet has decreased.

Even though significant performance benefits can be achieved by reducing tip clearance, it is practically impossible to reduce the tip clearance beyond a certain point. If the tip clearance is made too small, any vibration on the system can result in the blade rubbing against the

shroud, which will not only affect the performance, but also the overall life of the MAV. Therefore, one needs to explore other ways of improving the design of the shrouded rotors.

### Effect of Diffuser Length

Table 2 shows the CFD predicted performance variation of the shrouded rotor as a function of shroud diffuser length. The collective angle of the rotor is set to  $22^\circ$ . The baseline case corresponds to 15% diffuser length. As observed by Pereira and Chopra (Ref. 8), the diffuser length is seen to have very little effect on the performance of the overall system. However, as the diffuser length increases, the rotor thrust decreases, while the shroud thrust increases. The reason for the differences can again be understood by looking at the azimuthal variation of the shroud thrust for various configurations, see Fig. 18. The difference between configurations having different diffuser lengths is seen to arise mainly at the  $90^\circ$

Table 2: CFD predicted performance of micro-scale shrouded rotor for different shroud diffuser lengths,  $22^\circ$  collective setting.

Diffuser length (% $D_t$ )	$C_T$ (rotor)	$C_T$ (shroud)	$C_T$ (total)	$C_P$ (total)
15.0	0.0180	0.0064	0.0244	0.00343
22.5	0.0174	0.0066	0.0240	0.00341
30.0	0.0170	0.0072	0.0242	0.00342

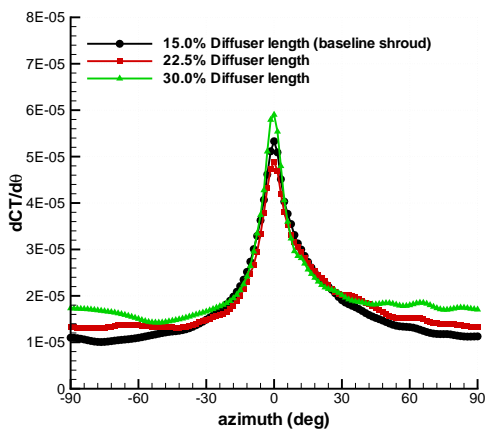
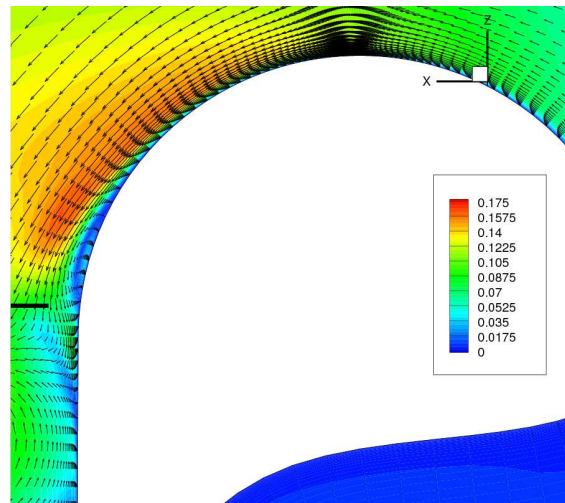
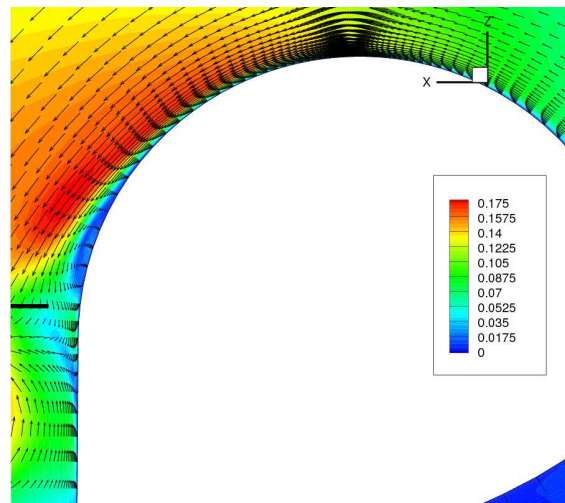


Figure 18: CFD predicted azimuthal variation of shroud thrust for different diffuser lengths,  $22^\circ$  collective setting.



(a) 15% diffuser length (baseline shroud)



(b) 30% diffuser length

Figure 19: Velocity magnitude (non-dimensionalized by tip speed) contour along with velocity vectors at  $90^\circ$  azimuth location for micro-scale shrouded rotor,  $22^\circ$  collective setting. Plane of the rotor is shown in black.

azimuth location. It is seen from Fig. 19, which shows the velocity magnitude (non-dimensionalized by tip speed) contour along with velocity vectors for the 15% (baseline) as well as the 30% diffuser length configurations, that the velocity at the inlet of the shroud is larger for the longer diffuser length configuration, thereby creating a larger suction pressure.

The contrast in the flow velocity over the shroud inlet for various shroud diffuser length configurations was found to be because of the difference in the wake trajectory (not shown). It was seen that the wake contracts at a slightly slower rate for the configuration with longer diffuser length. As a result, when the diffuser length is

longer, the tip vortex remain much closer to the shroud surface and the low pressure created by the tip vortex provides larger acceleration to the flow. The increase in the shroud contribution to the total thrust because of the smaller wake contraction can be explained independent of the above discussion, by using the momentum theory (Ref. 23) (discussed earlier).

In summary to this section, even though an increase in shroud thrust was achieved with longer diffuser length shrouds, the difference was just sufficient to compensate the decrease in rotor thrust. As a result, an increase in diffuser length did not have any effect on the performance of the chosen shrouded rotor. In reality, an increase in diffuser length will add to the weight of the shroud and therefore, has an adverse effect. Further studies are required to determine the shortest possible diffuser length that can be used for the shroud without compromising on the performance.

### Effect of Diffuser Angle

Table 3 shows the CFD predicted performance variation of the shrouded rotor as a function of shroud diffuser angle. The collective angle of the rotor is set to  $22^\circ$ . The baseline case corresponds to  $0^\circ$  diffuser angle. The overall performance remains the same with increasing diffuser angle, which is contrary to the observation made by Pereira and Chopra (Ref. 8). In the experiments of Pereira and Chopra, the best performance was obtained at a  $10^\circ$  diffuser angle.

The azimuthal variation of the shroud thrust in Fig. 20 shows marginal difference in the sectional thrusts for different diffuser angle configurations. As the diffuser angle is increased, the peak thrust increases marginally, while the thrust at the  $90^\circ$  azimuth decreases slightly. The differences could be understood by looking at the pressure contour plots, shown in Fig. 21, for the  $10^\circ$  shroud diffuser angle configuration. The pressure contours for the configurations with other diffuser angles ( $5^\circ$  and  $15^\circ$ ) are

Table 3: CFD predicted performance of micro-scale shrouded rotor for different shroud diffuser angles,  $22^\circ$  collective setting.

Diffuser angle ( $^\circ$ )	$C_T$ (rotor)	$C_T$ (shroud)	$C_T$ (total)	$C_P$ (total)
0	0.0180	0.0064	0.0244	0.00343
5	0.0180	0.0063	0.0243	0.00343
10	0.0179	0.0063	0.0242	0.00343
15	0.0179	0.0063	0.0242	0.00343

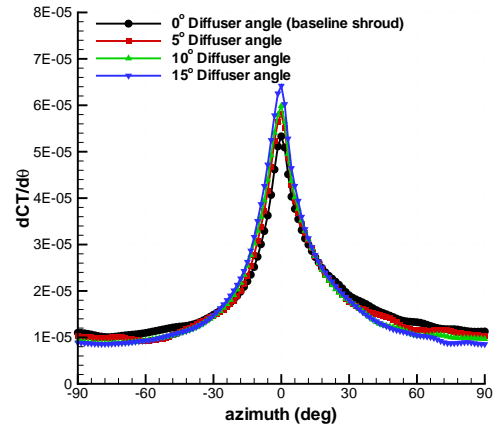


Figure 20: CFD predicted azimuthal variation of shroud thrust for different diffuser angles,  $22^\circ$  collective setting.

similar to that shown in Fig. 21, which is in turn similar to the pressure contours for the  $0^\circ$  diffuser angle (see Fig. 11). From the plot, it can be seen that the diffuser portion has high pressure at  $0^\circ$  and low pressure at  $90^\circ$  azimuth location. With increasing diffuser angle, the high pressure at the  $0^\circ$  azimuth produces additional thrust, while the low pressure at the  $90^\circ$  azimuth location reduces the sectional thrust. It should be kept in mind that use of very large diffuser angle might result in poorer performance because of flow separation.

Although no performance difference is seen by using a diffuser angle for this configuration, such a result may not be expected for all other shroud configurations. For a configuration, where the wake does not contract as much as for the present configuration, an angled diffuser might affect the overall performance.

### Effect of Shroud Inlet Shape

This section studies the effect of shroud inlet shape on the performance of the shrouded rotor. Four different elliptic shapes, 1.25 : 1, 1.5 : 1, 1.75 : 1 and 2 : 1 were studied. Note that, the baseline shroud inlet is circular. All the shrouds have equal minor axis length, while the major axis is varied according to the ratio provided. The cross section of 1.5 : 1 and 2 : 1 elliptic inlet shrouds along with the baseline configuration are shown in Fig. 22. Table 4 shows the CFD predicted performance of various shrouded rotor configurations at  $22^\circ$  collective setting. Clearly, the total thrust increases for shrouds with longer major axis, while the total power remains fairly constant. The rotor thrust decreases with increasing the major axis length and the shroud thrust more than compensates for the deficit. The variation of figure of merit (calculated

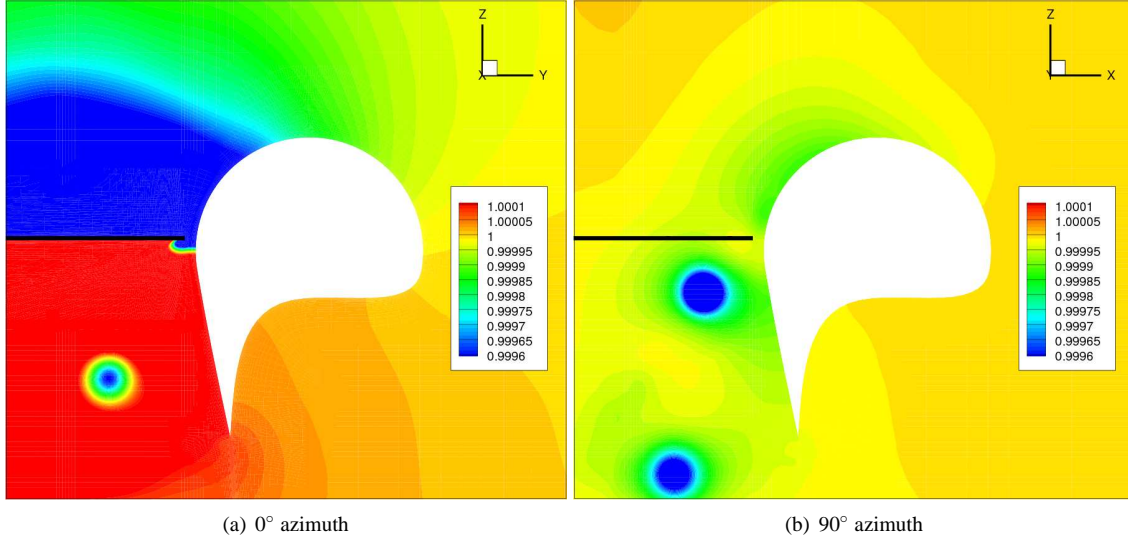


Figure 21: Sectional pressure (non-dimensionalized by freestream value) contour at different azimuth location for micro-scale shrouded rotor configuration with  $10^\circ$  diffuser angle,  $22^\circ$  collective setting. Plane of the rotor is shown in black.

based on ideal power for a free rotor operating at the same thrust) for various configurations, plotted in Fig. 23, shows that the  $FM$  reaches to a value greater than 0.9 for the 2 : 1 elliptic inlet shrouded rotor. The performance gain is larger than what was obtained by halving the tip clearance. The only penalty to be paid is a slightly larger shroud weight. Since the CFD predictions show that there is more scope of improvement by further elongating the elliptic inlet, this needs to be carefully studied experimentally in the future.

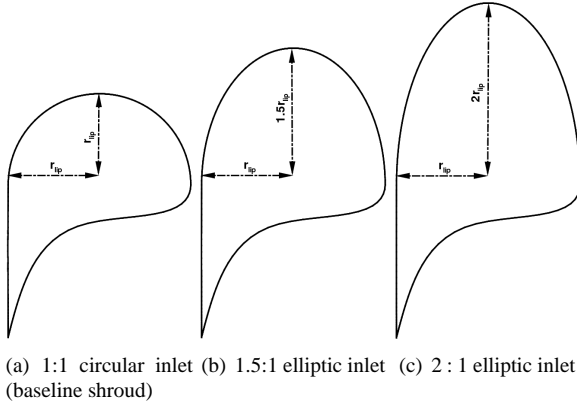


Figure 22: Cross-section of various shroud inlet shapes.

A better understanding of the differences in the shroud thrust for different shroud leading edge shapes can be obtained by looking at the azimuthal variation of the shroud thrust at one instant of time, see Fig. 24. Clearly, as the shroud inlet is elongated, both the peak at  $0^\circ$  azimuth,

Table 4: CFD predicted performance of micro-scale shrouded rotor for different shroud inlet shapes,  $22^\circ$  collective setting. Inlet shape defined by the ratio of major to minor axis of the ellipse.

Inlet Shape	$C_T$ (rotor)	$C_T$ (shroud)	$C_T$ (total)	$C_P$ (total)
1 : 1	0.0180	0.0064	0.0244	0.00343
1.25 : 1	0.0174	0.0074	0.0248	0.00347
1.5 : 1	0.0167	0.0087	0.0254	0.00346
1.75 : 1	0.0160	0.0103	0.0263	0.00344
2 : 1	0.0160	0.0110	0.0270	0.00344

as well as the base value at  $90^\circ$  azimuth increases. This suggests that, the difference between various shroud inlet shapes arise due to the variation in the amount of acceleration of the flow around the shroud leading edge, which is confirmed in Fig 25. Figure 25 shows the sectional pressure (non-dimensionalized by freestream value) contours along with velocity vectors at  $0^\circ$  and  $90^\circ$  for the configuration using 2 : 1 elliptic inlet shroud. The low pressure prevalent over the shroud inlet due to the flow acceleration is clearly visible at  $90^\circ$  azimuth. The velocity vectors also show a large region of separation.

Figure 26 compares the radial variation of non-dimensional pressure on the shroud for the baseline as well as the 2 : 1 elliptic inlet shroud configurations at  $0^\circ$  and  $90^\circ$  azimuth locations. The plot is similar to

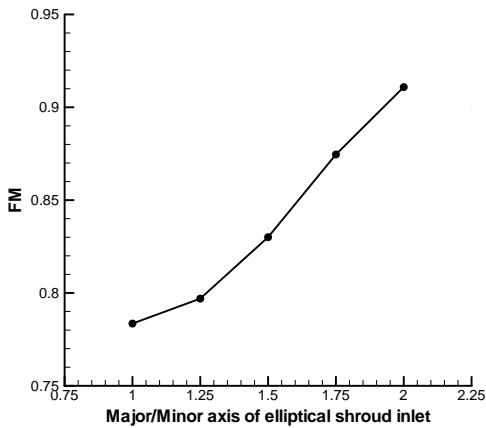


Figure 23: CFD predicted variation of figure of merit with shroud inlet profile,  $22^\circ$  collective setting.

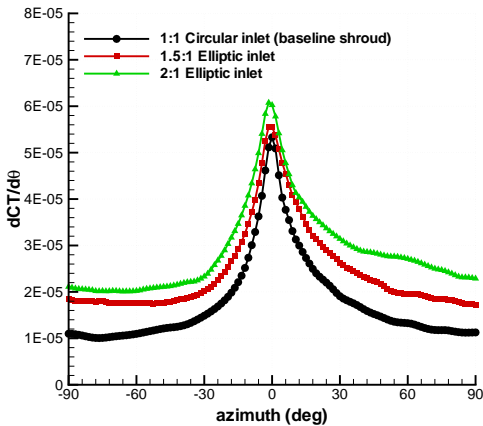


Figure 24: CFD predicted azimuthal variation of shroud thrust for different shroud inlet profiles,  $22^\circ$  collective setting.

that shown in Fig. 12(b). The radial location is non-dimensionalized by the minor axis of the shroud. For the 2 : 1 elliptic inlet shroud configuration, the decrease in pressure near the leading edge is very rapid as compared to the baseline shroud, which then becomes fairly constant when the flow separates. Even with the increased flow-separation, the extra thrust produced due to the low pressure near the leading edge for the 2 : 1 elliptic inlet shroud is sufficient to out-perform the baseline shroud.

A better understanding of the flow-field for an elliptic inlet shroud configuration can be obtained by looking at the wake velocities and the tip vortex trajectories. Figure 27 shows the radial variation of inflow and radial component of velocity averaged in the azimuthal direc-

tion for the 2 : 1 elliptic shroud inlet configuration. The variation is shown at different planes above and below the rotor. The plot is similar to that shown in Figs. 7 and 8 for the baseline configuration. The inflow produced by this 2 : 1 elliptic shroud inlet configuration, especially one chord above and in the plane of the rotor, is much larger compared to that from the baseline shroud geometry, which explains the reduced thrust produced by the rotor. The inflow produced near the root of the rotor and inboard is particularly larger than that from the baseline shrouded rotor or the free rotor. The radial component of velocity, on the other hand, is lower at all planes, resulting in a more vertically downward flow.

Figure 28 shows the wake trajectory produced by the rotors for the two different elliptic shroud inlet configurations along with that for the baseline configuration. In agreement with the earlier discussion on wake trajectory, the wake for the rotor with the most elongated shroud inlet, which provides the best shroud sharing of the total thrust, is observed to contract the least. In addition, the wake also convects down slower, even though the inflow is larger; in fact for the first 40 degrees of wake age, the tip vortex does not convect downward and it is only around 60 degrees of wake age that the tip vortex actually passes below the plane of the rotor. This is possibly caused by the smaller contraction rate, which places the tip vortex outside of the high inflow region and close to the shroud wall; image vortices would then act to slow down the downward trajectory. As a result of the lower contraction and vertical convection, the effect of tip vortex at the shroud inlet is more significant for the elongated inlets.

## Modified Elliptic Inlet Shroud

From all the calculations in the previous section, it is clear that the outer portion of the shroud does not contribute to the overall performance. However, this holds true only under hovering conditions. For forward flight conditions or even for hovering flight in the presence of gust, the outer portion of the shroud can play a significant role in the performance. A non-aerodynamic outer portion of the shroud can significantly increase the drag. In the current section, we propose a shroud design that uses the 2 : 1 elliptic inlet (which provided the best performance), but has a more aerodynamic outer portion. The inside portion of this shroud is similar to the original 2 : 1 elliptic inlet shroud. At the leading edge of the shroud, the ellipse from the inside portion is transformed to a circle with radius equal to the radius of curvature of the ellipse at that point. Following a  $90^\circ$  arc of this circle, a spline is fit to close the trailing edge. The cross-section of the proposed shroud along with the original 2 : 1 elliptic inlet shroud is shown in Fig. 29. For ease of reference, this modified

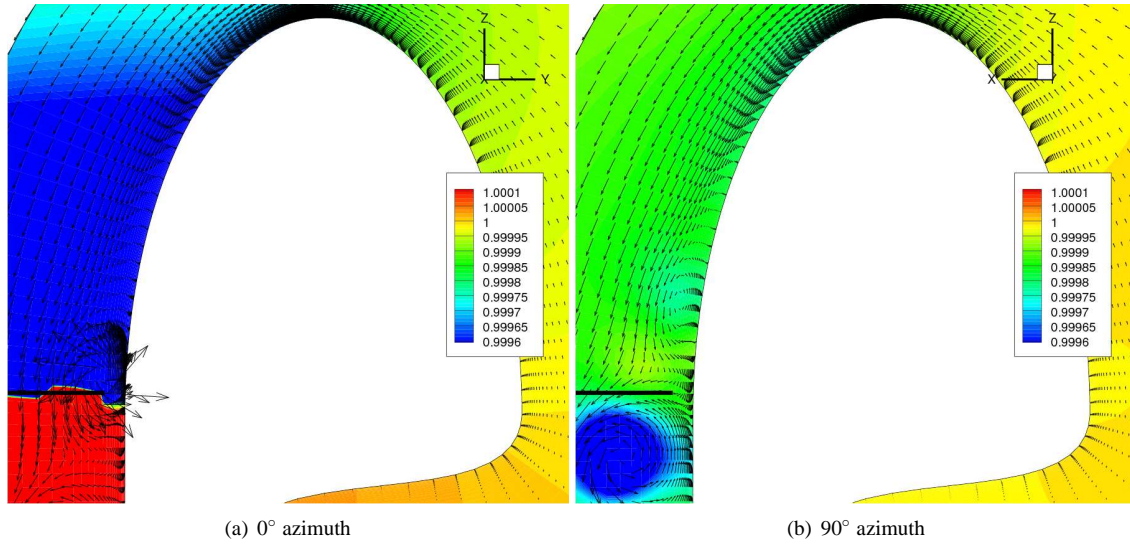


Figure 25: CFD predicted sectional pressure (non-dimensionalized by freestream value) contour at different azimuth location for 2 : 1 elliptic inlet shroud configuration, 22° collective setting. Plane of the rotor is shown in black.

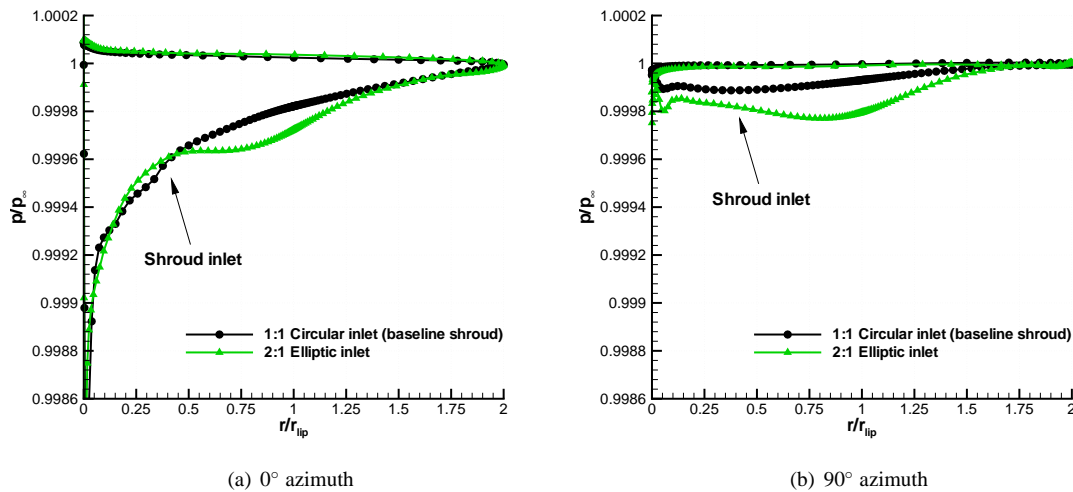


Figure 26: CFD predicted sectional pressure (non-dimensionalized by freestream value) distribution on shroud, 22° collective setting.

geometry will be referred to as 2 : 1 elliptic+circle inlet shroud.

Figure 30 shows the sectional pressure (non-dimensionalized by freestream value) contours along with velocity vectors at 0° and 90° for the configuration using 2 : 1 elliptic+circle inlet shroud. The collective setting is 22° and the RPM is 2500. When Fig. 30 is compared to a similar plot for the 2 : 1 elliptic inlet shroud configuration, shown in Fig. 25, it can be seen that they are nearly identical inside the shroud and very similar on the outer portion despite the large change in the outer

shroud geometry.

Following this, a collective angle sweep was performed for the configuration using the 2 : 1 elliptic+circle inlet shroud. The RPM was fixed at 2500. Figure 31(a) shows the power polar for both the 2 : 1 elliptic+circle inlet shroud and the baseline shroud configurations. In addition, the power polar for the free rotor is plotted for reference. The performance benefits obtained from using the elliptic inlet shroud is clearly visible. Note that, the power required for both the shrouded configurations are almost similar except at the collective angle of

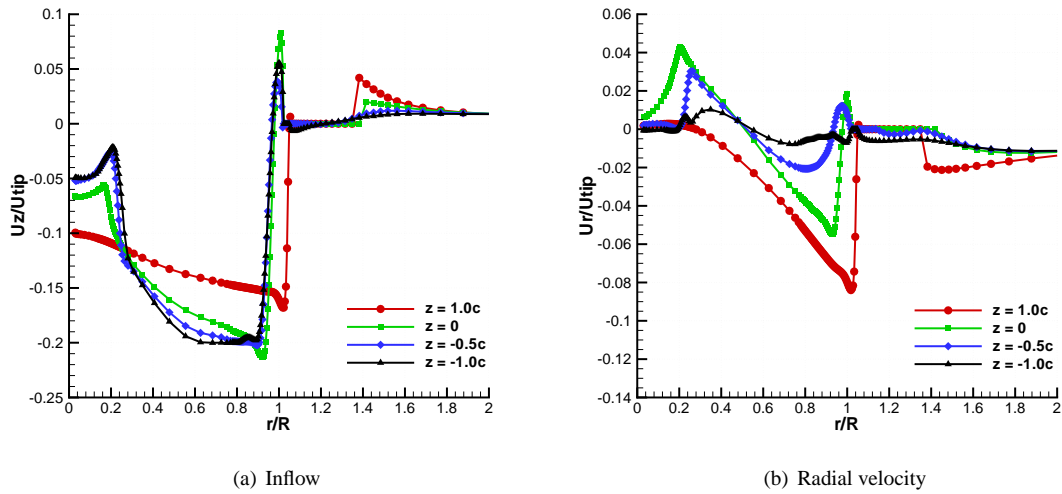


Figure 27: CFD predicted average wake velocity components (non-dimensionalized by tip speed) along radial direction at different planes above and below the rotor for 2 : 1 elliptic inlet shroud configuration, 22° collective setting.

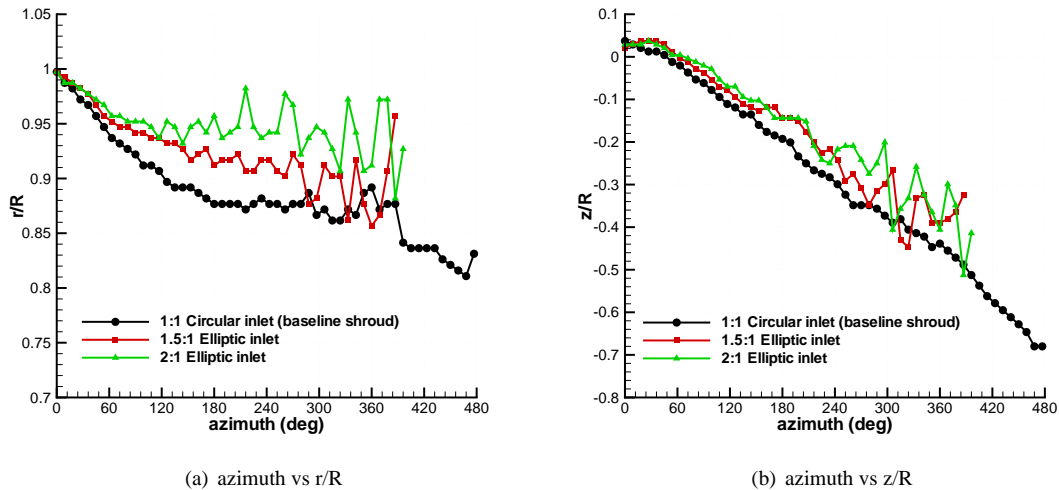


Figure 28: CFD predicted wake trajectory for micro-scale shrouded configuration with different shroud inlet profiles, 22° collective setting.

30°. At 30° collective setting, the baseline shroud configuration shows larger power due to the commencement of flow separation on the blade. On the other hand, the flow on the blade of the 2 : 1 elliptic+circular inlet shroud configuration remains attached even at these high collective angles due to smaller effective angles of attack seen by the blade sections, resulting from the increased inflow velocities at the plane of the rotor. As a result, the 2 : 1 elliptic+circular inlet shroud configuration shows good performance over a larger range of collective angles compared to the baseline configuration. It should be men-

tioned here that the performance of the configuration using 2 : 1 elliptic+circular inlet shroud at 22° collective setting is very similar to that of the configuration using original 2 : 1 elliptic inlet shroud. The modified shrouded configuration produces ~ 1% lower thrust compared to the original 2 : 1 elliptic inlet shroud configuration. Figure 31(b) plots the contribution of the shroud to the total thrust as a function of collective setting for both the 2 : 1 elliptic+circular inlet shroud and the baseline shroud configurations. The contribution of the shroud using the new geometry is much higher compared to that using the base-

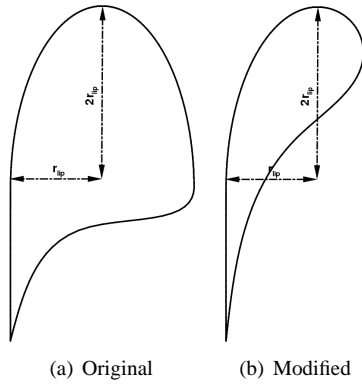


Figure 29: Cross-section of original and modified 2 : 1 elliptic shroud inlet shape.

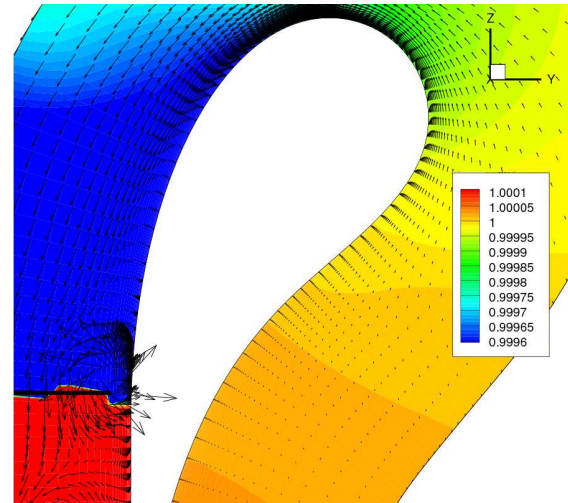
line shroud. For the 2 : 1 elliptic+circular inlet shroud configuration, the shroud contributes to more than 45% of the total thrust at 30° collective angle.

Figures 31(c) and (d), respectively, show the variation of figure of merit (calculated based on ideal power for a free rotor operating at the same thrust) and the ratio of thrust to power coefficient as a function of thrust coefficient. The improved performance of the 2 : 1 elliptic+circular inlet shroud configuration is clearly reflected in both the plots, especially at higher thrust values. The maximum figure of merit increases to about 0.98 for the 2 : 1 elliptic+circular inlet shroud configuration and occurs at a higher thrust level than for the baseline configuration. The maximum power loading is nearly identical for the 2 : 1 elliptic+circular inlet shroud configuration as for the baseline configuration; however, it remains close to its maximum value for a very large range of thrust for the 2 : 1 elliptic+circular inlet shroud configuration. To clarify, one should not be surprised to see such high values of  $FM$ , since the  $FM$  is calculated based on the ideal power for a free rotor and not for a ducted rotor. Using this definition, the  $FM$  can even have a value greater than 1. Defining  $FM$  based on the ideal power for a free rotor provides a fair parameter to compare the performances of various configurations.

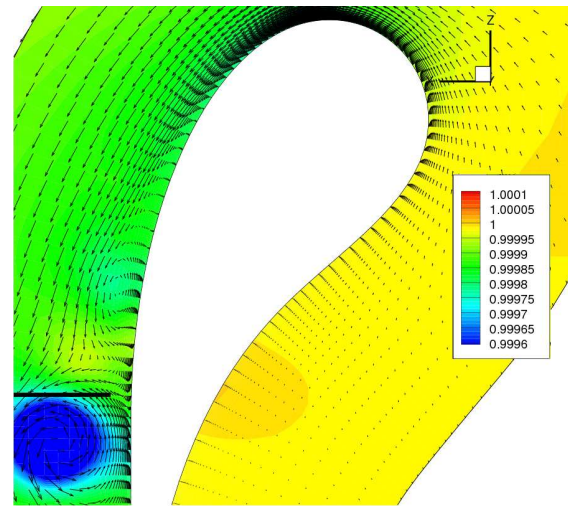
The analysis clearly demonstrates the performance benefits obtained in hover for a configuration using an elliptic inlet shroud as compared to the free rotor or the configuration using a circular inlet shroud. Further studies are necessary to determine the advantages or disadvantages of using the proposed shroud design in non-hovering flight conditions.

## Summary

A compressible Reynolds-Averaged Navier-Stokes (RANS) solver was applied to simulate the aerody-



(a) 0° azimuth



(b) 90° azimuth

Figure 30: CFD predicted sectional pressure (non-dimensionalized by freestream value) contour at different azimuth location for 2 : 1 elliptic+circular inlet shroud configuration, 22° collective setting. Plane of the rotor is shown in black.

namics of micro-scale shrouded rotor configuration in hover. The computations were performed on structured body-conforming blade and shroud meshes, overset in a cylindrical background mesh. The computations were validated with experimentally measured mean thrust and power and a detailed understanding of the flow physics was attained. Additionally, the effect of various shroud parameters such as tip clearance, diffuser length, diffuser angle and shroud inlet shape on the performance were studied. The following are specific conclusions that can be drawn from the present work :

1. The overall performance is well predicted for a

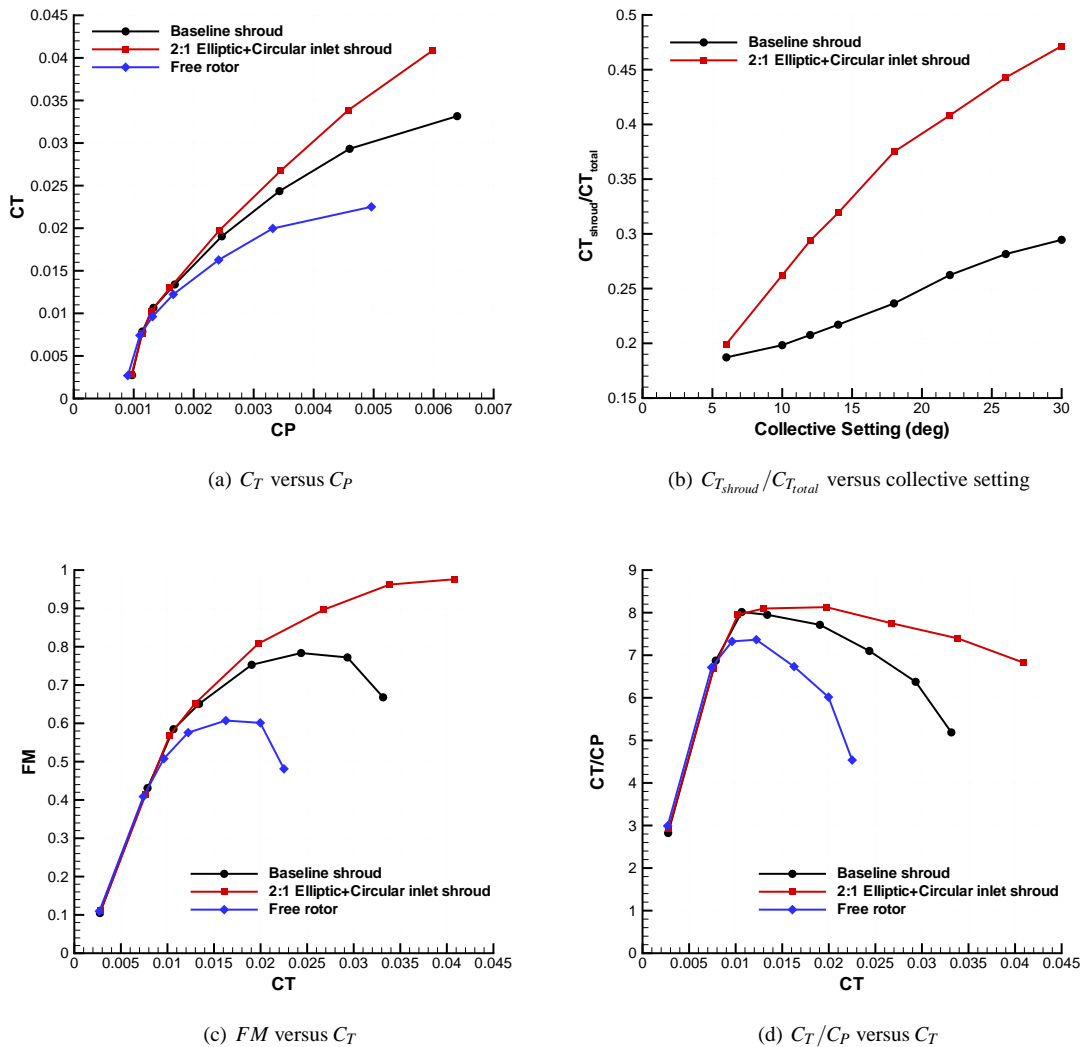


Figure 31: CFD predicted performance at different collective settings for 2 : 1 elliptic+inlet shroud configuration along with that of baseline shroud and free rotor configurations.

range of RPMs. Shrouded rotor configuration generates larger thrust compared to the free rotor, while power required for both the configurations are not too different. The difference in the computed power for the free and the shrouded configuration is less than 4% at all rotational speeds.

2. Collective angle sweep study showed that the shrouded rotor produce higher thrust compared to the free rotor at all collective settings, with the difference more pronounced at higher values ( $\sim 30\%$  higher at  $26^\circ$  collective angle compared to  $\sim 8\%$  higher at  $14^\circ$  collective angle). The thrust produced by the rotor in the shrouded configuration is lower than that produced by the free rotor. However, the

thrust produced by the shroud more than compensates for the deficit. The contribution of shroud to the total thrust increases from about 19% at lower collective setting to as high as 29% at the highest collective setting. The power required for both the free as well as the shrouded rotors are almost identical (within 5%) at all collective settings.

3. The inflow at different planes above and below the rotor is larger for the shrouded configuration compared to the free rotor. As a result, the rotor in the shrouded configuration produces lower thrust throughout the span. The power distribution, on the other hand, is comparable, with marginal differences in the outboard region. The shape of the thrust and

power distributions along the span of the blade are not too different between free and shrouded rotors, suggesting that the performance of the rotor blade might be optimized separately from the shroud geometry.

4. The thrust produced from the shroud is identified to come from two main sources. First, the low pressure created primarily by the blades and partly by the tip vortex around the shroud inlet generates large shroud thrust at sections near the blade location. Second, the suction created due to the flow accelerating around the shroud inlet generates additional thrust, and becomes the primary source of thrust production at shroud sections away from the blades. The low pressure due to the tip vortex can help in enhancing the flow acceleration.
5. The wake contracts at a much slower rate for the shrouded rotor as compared to from a free rotor. As a general trend, increased shroud performance comes with smaller wake contraction, which agrees with the momentum theory.
6. Decreasing the tip clearance of the shroud improved the performance of shrouded rotor significantly. The configuration with tip clearance of half that of the baseline shroud improved the  $FM$  by more than 10%. Reducing the tip clearance increases both the low pressure created by the blade on the shroud inlet as well as the suction created by the flow acceleration on the shroud.
7. Diffuser length and diffuser angle did not have any effect on the performance of the shroud. Increasing the diffuser length increases the shroud thrust, but the gain is just sufficient to balance the decrease in rotor thrust.
8. Changing the inlet shape of the shroud from circular to elliptical improved the performance of the shrouded configuration significantly. The configuration using 2 : 1 elliptic inlet shroud achieved about 18% improvement in  $FM$  compared to the baseline configuration. The improvement is achieved because of the larger suction created by increased flow acceleration around the shroud leading edge. The inflow when using elliptic inlet shroud was seen to be much larger compared that using the baseline shroud.
9. An improved aerodynamic shroud design was proposed, which has elliptic shape on the inner portion of the shroud inlet and a circular shape on the outer portion. The hover performance of the configuration using this shroud was not too different from

the original elliptic inlet shroud. However, the new shroud design can be expected to perform better in non-hovering flight conditions.

10. Collective angle sweep study showed that the improved proposed shroud provided significant performance benefits. The maximum  $FM$  (based on ideal power of the free rotor) was seen to increase to approximately 0.98 as compared to 0.78 for the baseline shroud and 0.60 for the free rotor. Furthermore, the contribution to thrust from the shroud increased from about 20% at lower collective setting to almost 48% at the higher collective setting. As a result the power loading curve remained close to its maximum value for a significant range of thrust.

As a concluding remark, it was seen that the performance of micro-scale shrouded rotors can be significantly improved by choosing appropriate shroud parameters. However, further studies are required to design an optimum shroud. The scope of current paper was limited to hover analysis. As a continuing work, studies will be done to understand the benefits or disadvantages of the proposed shroud design in non-hovering conditions such as forward flight, ascending or descending flight etc. In addition, efforts will be made to optimize the major to minor axis ratio of the elliptic inlet. Future work will also look at including linear twist to the blade, since that was shown to improve the rotor performance in an earlier paper by the current authors (Ref. 12).

## Acknowledgments

This work was supported by Army's MAST-CTA center on Microsystem Mechanics, Technical Monitor Dr. Joseph Mait. Authors would like to thank Vikram Hrishikeshavan for providing the experimental data.

## References

- <sup>1</sup>Sacks, A. H., and Burnell, J. A., "Ducted Propellers—A Critical Review of the State of the Art," *Progress in Aeronautical Sciences*, edited by A. Ferri, D. Kuchemann, and L. H. G. Sterne, Vol. 3, Part 2, Pergamon Press, New York, NY, 1962, pp. 85–135.
- <sup>2</sup>Mouille, R., and d'Ambra, F., "The "Fenestron" A Shrouded Tail Rotor Concept for Helicopters," American Helicopter Society 42nd Annual Forum Proceedings, Washington, D.C., June 2–5, 1986.
- <sup>3</sup>Andrews, III, J. R., Riley, Jr., R. G., and Rahnke, C., "Design and Testing of a Ducted Tail Rotor Concept Demonstrator for a Model 222U Helicopter," Pa-

per No. 4, Twenty-Second European Rotorcraft Forum, Brighton, U.K., Sep 16–19, 1996.

<sup>4</sup>Kruger, W., “On Wind Tunnel Tests and Computations Concerning the Problem of Shrouded Propellers,” NACA TM 1202, Feb 1949. Translation of ZWB Forschungsbericht Nr. 1949, Aerodynamischen Versuchsanstalt (AVA), Göttingen, Germany, Jan 21, 1944.

<sup>5</sup>Parlett, L. P., “Aerodynamic Characteristics of a Small-Scale Shrouded Propeller at Angles of Attack from 0 to 90,” NACA TN 3547, Langley Memorial Aeronautical Laboratory, Langley Field, VA, Nov 1955.

<sup>6</sup>Lipera, L., “MicroCraft Ducted Air Vehicle,” Micro Craft Inc., San Diego, Internal Report, 2001.

<sup>7</sup>Walsh, D., and Cycon, J. P., “The Sikorsky Cypher UAV: A Multi-purpose Platform with Demonstrated Mission Flexibility,” American Helicopter Society 54th Annual Forum Proceedings, Washington, D.C., May 20–22, 1998.

<sup>8</sup>Pereira, J., and Chopra, I., “Hover Tests of Micro Aerial Vehicle-Scale Shrouded Rotors, Part I: Performance Characteristics,” *Journal of the American Helicopter Society*, Vol. 54, (1), January 2009.

<sup>9</sup>Pereira, J., and Chopra, I., “Hover Tests of Micro Aerial Vehicle-Scale Shrouded Rotors, Part II: Flow Field Measurements” *Journal of the American Helicopter Society*, Vol. 54, (1), January 2009.

<sup>10</sup>Hrishikeshavan, V. and Chopra, I., “Design and Testing of a Shrouded Rotor Micro Air Vehicle with Anti-torque Vanes,” American Helicopter Society 64th Annual Forum Proceedings, Montréal, Quebec, Canada, April 29–May 1, 2008.

<sup>11</sup>Lakshminarayan, V. K., and Baeder, J. D., “Computational Investigation of Micro Hovering Rotor Aerodynamics,” To appear in *Journal of the American Helicopter Society*, Vol. 55, No. 2, April 2010.

<sup>12</sup>Lakshminarayan, V. K., and Baeder, J. D., “Numerical Study of the Effects of Leading and Trailing Edge Geometries and Planform on Micro Hovering Rotor,” American Helicopter Society International Specialists’ Meeting on Unmanned Rotorcraft, Phoenix, AZ, January 20–22, 2009.

<sup>13</sup>Lummer, D. T., “CFD Investigation of a Hovering Micro-Air Vehicle,” Scholarly Paper, Department of Aerospace Engineering, University of Maryland at College Park, 2008.

<sup>14</sup>Lakshminarayan, V. K., “Computational Investigation of Micro-Scale Coaxial Rotor Aerodynamics in Hover,” Ph.D. dissertation, Department of Aerospace Engineering, University of Maryland at College Park, 2009.

<sup>15</sup>Buelow, P. E. O., Schwer, D. A., Feng, J., and Merkle, C. L., “A Preconditioned Dual-Time, Diagonalized ADI scheme for Unsteady Computations,” AIAA paper 1997-2101, 13th AIAA Computational Fluid Dynamics Conference, Snowmass Village, CO, June 29–July 2, 1997.

<sup>16</sup>Pandya, S. A., Venkateswaran, S., and Pulliam, T. H., “Implementation of Preconditioned Dual-Time Procedures in OVERFLOW,” AIAA paper 2003-0072, 41st AIAA Aerospace Sciences Meeting and Exhibit, Reno, NV, January 6–9, 2003.

<sup>17</sup>Pulliam, T., and Chaussee, D., “A Diagonal Form of an Implicit Approximate Factorization Algorithm,” *Journal of Computational Physics*, Vol. 39, (2), February 1981, pp. 347–363.

<sup>18</sup>Turkel, E., “Preconditioning Techniques in Computational Fluid Dynamics,” *Annual Review of Fluid Mechanics*, Vol. 31, January 1999, pp. 385–416.

<sup>19</sup>Spalart, P. R., and Allmaras, S. R., “A One-equation Turbulence Model for Aerodynamic Flows,” AIAA Paper 1992-0439, 30th AIAA Aerospace Sciences Meeting and Exhibit, Reno, NV, January 6–9, 1992.

<sup>20</sup>Duraisamy, K., “Studies in Tip Vortex Formation, Evolution and Control,” Ph.D dissertation, Department of Aerospace Engineering, University of Maryland. College Park, MD. 2005.

<sup>21</sup>Srinivasan, G. R., and Baeder, J. D., “TURNS: A Free-wake Euler/ Navier-Stokes Numerical method for Helicopter Rotors,” *AIAA Journal*, Vol. 31, No. 5, May 1993, pp. 959–962.

<sup>22</sup>Lee, Y., “On Overset Grid Connectivity and Automated Vortex Tracking in Rotorcraft,” Ph.D dissertation, Department of Aerospace Engineering, University of Maryland. College Park, MD. 2008.

<sup>23</sup>Leishman, J. G., *Principles of Helicopter Aerodynamics*, Cambridge University Press, New York, NY, 2002.

<sup>24</sup>Jeong, J. and Hussain, F., “On the Identification of a Vortex,” *Journal of Fluid Mechanics*, Vol. 285, 1995, pp. 69–94.